ACS Catalysis

pubs.acs.org/acscatalysis Research Article

Reducibility and Dispersion Influence the Activity in Silica-Supported Vanadium-Based Catalysts for the Oxidative Dehydrogenation of Propane: The Case of Sodium Decavanadate

Manouchehr Nadjafi, Paula M. Abdala, Rene Verel, Davood Hosseini, Olga V. Safonova, Alexey Fedorov,* and Christoph R. Müller*

Cite This: *ACS Catal.* 2020, 10, 2314−2321 Read Online

ACCESS | Metrics & More | Article Recommendations | Supporting Information

ABSTRACT: Calcined silica-supported sodium decavanadate ($Na_6V_{10}O_{28}/SiO_2$) is more active for the oxidative dehydrogenation of propane (ODP) than the thermodynamically stable α-polymorph of sodium metavanadate (α-$NaVO_3/SiO_2$) and the silica-bound, site-isolated terminal vanadium oxo $[VO_4]/SiO_2$ benchmark catalyst. Calcination of $Na_6V_{10}O_{28}/SiO_2$ in air at 600 °C leads to a mixture of $Na_{1+x}V_3O_8$, interacting with the silica support, and the metastable polymorph of sodium metavanadate, β-$NaVO_3$. The formation of β-$NaVO_3$ at this temperature is unexpected as β-$NaVO_3$ supported on silica and calcined at the same conditions transforms into α-$NaVO_3$. At 450 °C (temperature of the ODP reaction) in an inert atmosphere, $Na_6V_{10}O_{28}/SiO_2$ transforms predominantly to the reduced phase α'-NaV_2O_5 that displays poor activity in ODP. However, the deactivated material recovers the high activity of calcined $Na_6V_{10}O_{28}/SiO_2$ after ca. 3 h time on stream (TOS) or after 1 h in air (450 °C). This observation is consistent with the proposed link between the high catalytic activity in ODP and the reducibility of a V phase as neither the catalytic performance nor characteristic Raman bands of α-$NaVO_3/SiO_2$ and $[VO_4]/SiO_2$ change significantly in an inert atmosphere at 450 °C. Vanadium K-edge operando X-ray absorption near-edge structure (XANES) and in situ Raman mapping show that the oxidation of α'-NaV_2O_5 to a mixture of $Na_{1+x}V_3O_8$ and β-$NaVO_3$ occurs under ODP conditions within several minutes. In contrast, the initial activity recovers within hours (depending on the conditions), and it is explained mostly by slow redispersion of the $Na_{1+x}V_3O_8$ phase on SiO_2.

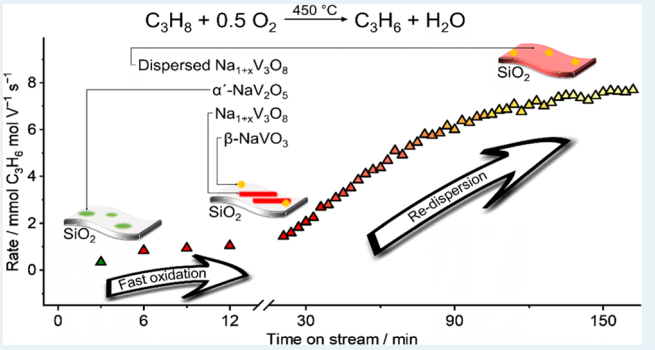

KEYWORDS: *polyoxovanadate, oxidative dehydrogenation of propane, reducible VO_x catalyst, β-$NaVO_3$, operando XANES*

INTRODUCTION

Oxidative dehydrogenation of propane (ODP, eq 1) is an "on-purpose" propene production technique that has several advantages relative to nonoxidative dehydrogenation of propane (PDH, eq 2). In particular, ODP is exothermic, it requires lower operating temperatures (ca. 400−500 vs 550−700 °C), features reduced coking due to the cofeeding of O_2, and it avoids thermodynamic product limitations (e.g., 37% at 550 °C for PDH).[1−3] However, a yet unsolved challenge in the ODP using V-based catalysts is overoxidation, i.e., the preferred oxidation of propene over propane, that hampers achieving high propene selectivities at high propane conversions.[1−5]

$$C_3H_8 + 0.5O_2 \rightarrow C_3H_6 + H_2O\ (\Delta H^0_{298K} = -117\ \text{kJ mol}^{-1}) \quad (1)$$

$$C_3H_8 \rightarrow C_3H_6 + H_2\ (\Delta H^0_{298K} = 124.6\ \text{kJ mol}^{-1}) \quad (2)$$

Supported vanadium oxide catalysts are among the most active[3] and most studied[5] ODP catalysts. However, the yield of and the selectivity to propene under ODP conditions are not yet sufficiently high to allow an industrial deployment of this technology.[3]

Solid-state ^{51}V NMR,[6−10] in situ X-ray absorption near-edge structure (XANES),[11,12] UV−vis,[12−14] and in situ Raman studies with ^{18}O isotopic labeling[15,16] have shown that, below a monolayer coverage, supported V_2O_5 species exist as $[VO_4]$ sites, i.e., surface-bound terminal oxo V^{5+} species ($(-O)_3V{=}O$),[17] as long as the support (TiO_2, ZrO_2, Al_2O_3, etc.) is dehydrated. Oligomeric $[VO_4]$ sites form at an increased vanadium loading, leading to a surface monolayer of vanadia

Received: November 3, 2019
Revised: January 17, 2020
Published: January 17, 2020

https://dx.doi.org/10.1021/acscatal.9b04752
ACS Catal. 2020, 10, 2314−2321

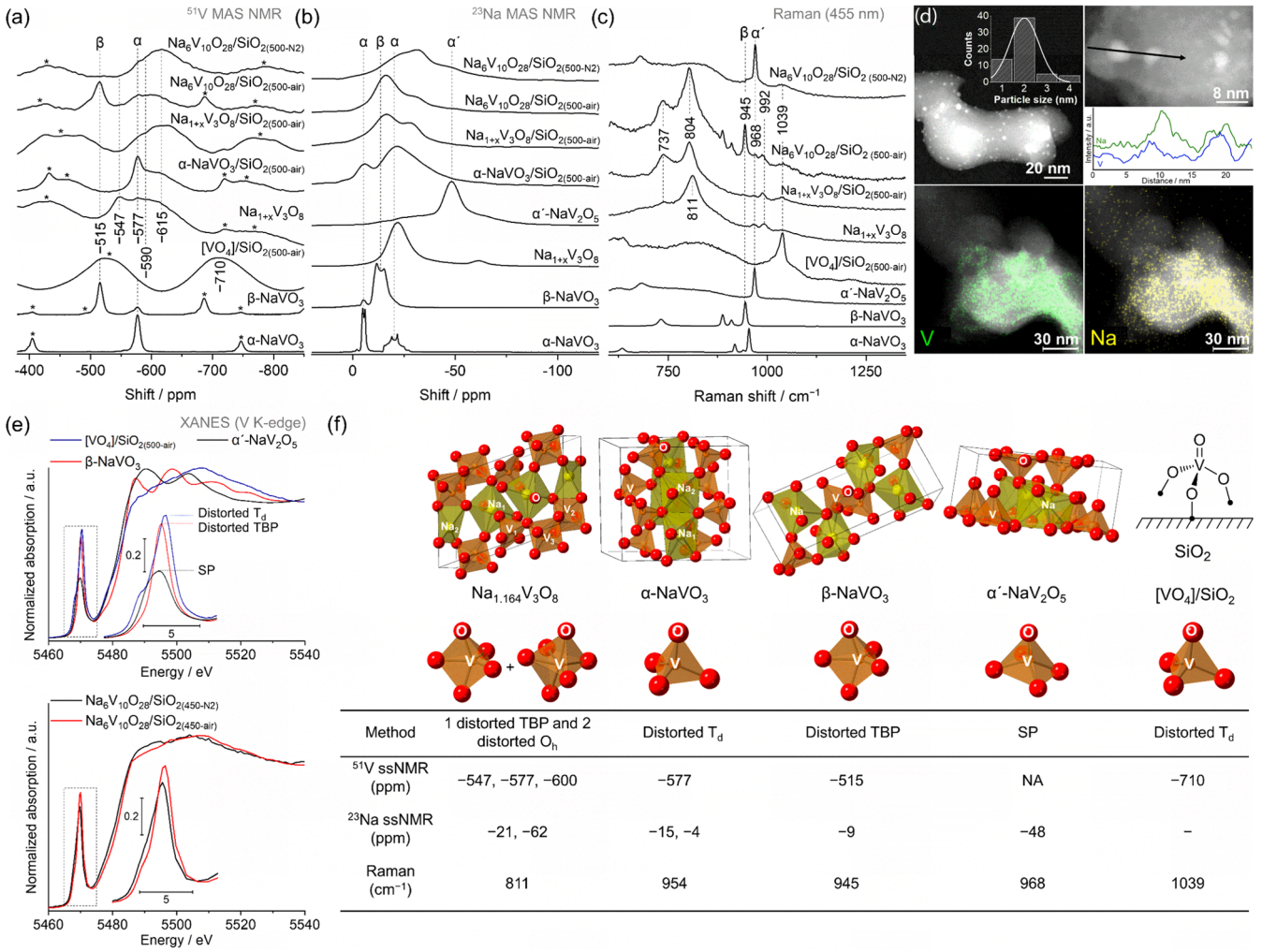

Method	1 distorted TBP and 2 distorted O_h	Distorted T_d	Distorted TBP	SP	Distorted T_d
^{51}V ssNMR (ppm)	−547, −577, −600	−577	−515	NA	−710
^{23}Na ssNMR (ppm)	−21, −62	−15, −4	−9	−48	–
Raman (cm^{-1})	811	954	945	968	1039

Figure 1. (a) ^{51}V and (b) ^{23}Na MAS NMR (15−18 kHz spinning rate, spinning side bands are marked by asterisks); (c) Raman spectra of calcined (air), dehydrated, and N_2-treated $Na_6V_{10}O_{28}/SiO_2$ along with the respective references (β-$NaVO_3$ and $Na_{1+x}V_3O_8$ references contain minor amounts of α-$NaVO_3$ and $NaV_{10}O_{15}$ impurities, respectively); (d) high-angle annular dark-field-TEM of $Na_6V_{10}O_{28}/SiO_2$ with line scan analysis and energy-dispersive X-ray (EDX) mapping; (e) V K-edge XANES of $Na_6V_{10}O_{28}/SiO_{2(450\text{-air})}$, $Na_6V_{10}O_{28}/SiO_{2(450\text{-}N_2)}$, and references; and (f) crystal structure, coordination environment of V, and characteristic peaks of selected characterization methods used in this study to distinguish different species.

or, at even higher loadings (>8−9 V nm^{-2} for oxide supports except for silica),[3,18−23] V_2O_5 nanoparticles, although properties of the support (composition, specific surface area, and synthesis method) also influence the nature of V surface species.[19,20,22−25] In general, the formation of V_2O_5 nanoparticles (>3 nm) correlates with reduced catalytic activity of V-based ODP catalysts.[3] V_2O_5 nanoparticles start to form on silica even at a submonolayer coverage (2.6−3.3 V nm^{-2}).[19,20,24,25] However, the addition of a sodium promoter improves the dispersion of vanadia on SiO_2, allowing for ca. 8.6 V nm^{-2}, while still avoiding the formation of V_2O_5 (~6.2 wt % V, 0.4 wt % Na^+), thereby enhancing ODP space−time yield (STY) in such promoted catalysts until crystalline V_2O_5 and sodium metavanadate start to form at Na^+ loadings of <0.4 and >1 wt %, respectively.[19] In addition to influencing the dispersion, a slight decrease in the turnover frequency (TOF) after promotion with sodium was observed for VO_x/SiO_2, presumably due to an interaction between Na^+ and vanadyl sites resulting in a weaker V═O bond.[26] Furthermore, it has been reported that alkali metal dopants (Li, Na, and K) decrease the activity of alumina-supported vanadium-based ODP catalysts,[27] presumably, by decreasing the reducibility of V sites that operate via a redox mechanism involving V^{5+} as the initial state and V^{3+} or V^{4+} intermediates.[3,5,28−37]

This work aims to provide insight into the relationship between structure, reducibility, dispersion, selectivity, and activity of sodium vanadate-based ODP catalysts. Silica was utilized as a support due to its inertness[19] (Al_2O_3, ZrO_2, or CeO_2 might react with a vanadium precursor forming $AlVO_4$, ZrV_2O_7, or $CeVO_4$, respectively)[3] and to minimize the X-ray absorption by the support to facilitate the operando XANES study (vide infra). To this end, sodium decavanadate clusters, i.e., $Na_6V_{10}O_{28}$, were dispersed on silica and calcined in air at 600 °C, yielding a mixture of β-$NaVO_3$ and $Na_{1+x}V_3O_8$ interacting with the silica support (this calcined material is denoted $Na_6V_{10}O_{28}/SiO_2$). The ODP activity of supported β-$NaVO_3$, a metastable polymorph of $NaVO_3$, has so far remained unexplored because the transformation of β-$NaVO_3$ to α-$NaVO_3$ occurs at lower temperatures than commonly used for ODP (in bulk materials at ca. 400 °C, Figures S1 and S2).[38]

https://dx.doi.org/10.1021/acscatal.9b04752
ACS Catal. 2020, 10, 2314−2321

We report that the specific activity of $Na_6V_{10}O_{28}/SiO_2$ is, respectively, 45 and 24% higher than that of α-$NaVO_3/SiO_2$ and the $[VO_4]/SiO_2$ reference catalysts at identical V loadings. This activity trend correlates with the higher reducibility of $Na_6V_{10}O_{28}/SiO_2$ as it readily converts to the α'-NaV_2O_5 phase on SiO_2 (formal oxidation state of 4.5) under N_2 flow at 450 °C. The easy reducibility could be linked to lower activation energies for accommodating various oxidation states and coordination geometries of the catalytic cycle for ODP. Experiments using operando XANES and in situ Raman scattering mapping show that the reduced α'-NaV_2O_5 phase is quickly reoxidized to β-$NaVO_3$ and $Na_{1+x}V_3O_8$ (in approximately 12 min) in ODP conditions. However, recovering the high activity of $Na_6V_{10}O_{28}/SiO_2$ takes ca. 3 h under reaction conditions, and it correlates, according to in situ Raman mapping and ex situ transmission electron microscopy (TEM) results, with the redispersion of $Na_{1+x}V_3O_8$ and β-$NaVO_3$ on the silica with time on stream (TOS). Only subtle changes in the pre-edge peak intensity and position in operando V K-edge XANES data were observed after the fast oxidation stage, which further reinforces the assertion that the redispersion of $Na_{1+x}V_3O_8$ and β-$NaVO_3$ with TOS (ca. 3 h) is the major driver for improving the catalytic activity of the reduced material with time on stream.

RESULTS AND DISCUSSION

Incipient wetness impregnation (IWI) of an aqueous solution of $Na_6V_{10}O_{28}$ onto silica (Aerosil 300, calcined at 600 °C, 286 $m^2\ g^{-1}$) gives $Na_6V_{10}O_{28}/SiO_{2(IWI)}$ with 2.0 wt % V loading as determined by inductively coupled plasma (ICP) analysis, corresponding approximately to 1 V nm^{-2}, which is well below the monolayer coverage limit of ca. 2.6 V nm^{-2} for silica using IWI.[12] Since the nature of the surface vanadium species changes with dehydroxylation,[39] we treated $Na_6V_{10}O_{28}/SiO_{2(IWI)}$ under a flow of synthetic air at 500 °C and then handled this dehydroxylated $Na_6V_{10}O_{28}/SiO_{2(500\text{-}air)}$ material for further characterization without exposure to air (such materials are labeled throughout the manuscript using subscript notations of the dehydroxylating temperature and the dehydroxylating gas).

Probing $Na_6V_{10}O_{28}/SiO_{2(500\text{-}air)}$ by ^{51}V MAS NMR reveals several characteristic signals including a peak at −515 ppm assigned to β-$NaVO_3$ (vanadium sites in a distorted trigonal bypiramidal geometry, TBP, Figure 1a).[40] The formation of the metastable β-sodium metavanadate polymorph in preference to the thermodynamically stable α-sodium metavanadate (vide infra) was unexpected. In addition to the peak at −515 ppm, there is a broad peak at ca. −600 ppm, reminiscent of crystalline $Na_{1+x}V_3O_8$ that also gives a broad peak at around −590 ppm (Figure 1a). A reference material containing $Na_{1+x}V_3O_8$ on silica at the same vanadium loading displays, after calcination and dehydration ($Na_{1+x}V_3O_8/SiO_{2(500\text{-}air)}$), a similar broad feature but is shifted further upfield, at ca. −615 ppm. While these peaks are similar in crystalline $Na_{1+x}V_3O_8$ as well as in $Na_{1+x}V_3O_8/SiO_{2(500\text{-}air)}$ and $Na_6V_{10}O_{28}/SiO_{2(500\text{-}air)}$, the peak positions in silica-supported materials are shifted upfield with respect to crystalline $Na_{1+x}V_3O_8$ by approximately 25 and 10 ppm, respectively, suggesting an interaction between sodium trivanadate and SiO_2. The nature of this interaction is likely related in both silica-supported materials, and the observed stronger upfield shift for $Na_{1+x}V_3O_8/SiO_{2(500\text{-}air)}$ relative to $Na_6V_{10}O_{28}/SiO_{2(500\text{-}air)}$ (Figure 1a) could be caused by the presence of β-$NaVO_3$ in $Na_6V_{10}O_{28}/SiO_{2(500\text{-}air)}$ or be due to the different Na/V ratios in these supported samples. We tentatively attribute the broad peaks at ca. −600 ppm in $Na_6V_{10}O_{28}/SiO_{2(500\text{-}air)}$ and −615 ppm in $Na_{1+x}V_3O_8/SiO_{2(500\text{-}air)}$ to $[VO_4]/SiO_2$ sites interacting with Na^+ cations because a similar feature was also observed as a broad shoulder at ca. −610 ppm in α-$NaVO_3/SiO_{2(500\text{-}air)}$. The latter material displays a major peak of crystalline α-$NaVO_3$ at −577 ppm (vanadium sites in a distorted T_d environment,[40] Figure 1a). Note that this characteristic peak of α-$NaVO_3$ is not clearly observed in $Na_6V_{10}O_{28}/SiO_{2(500\text{-}air)}$ or $Na_{1+x}V_3O_8/SiO_{2(500\text{-}air)}$. At last, while the reference $[VO_4]/SiO_{2(500\text{-}air)}$ (2.1 wt % V by ICP, ca. 1 V nm^{-2}) features a broad peak at ca. −710 ppm[8,25] (Figure 1a), the interaction of $[VO_4]/SiO_2$ with Na^+ was reported to shift this peak downfield to −675 ppm at a Na/V molar ratio of 0.2.[19] The difference in the peak position for $[VO_4]\cdots Na^+$ sites observed in this work and in the literature could be due to the different nature and amount of the sodium phase used.[19]

^{23}Na MAS NMR spectrum of $Na_6V_{10}O_{28}/SiO_{2(500\text{-}air)}$ shows two major peaks similar to those found for $Na_{1+x}V_3O_8/SiO_{2(500\text{-}air)}$, indicating similar sodium environments in these two materials. However, the intensity of a more deshielded peak at −16 ppm in $Na_6V_{10}O_{28}/SiO_{2(500\text{-}air)}$ is increased compared to that in $Na_{1+x}V_3O_8/SiO_{2(500\text{-}air)}$, and this is explained by the overlapping ^{23}Na signal of the β-$NaVO_3$ phase that is present in $Na_6V_{10}O_{28}/SiO_{2(500\text{-}air)}$ (Figure 1b). The splitting of the main peak of crystalline $Na_{1+x}V_3O_8$ at around −21 ppm into two Na environments in $Na_{1+x}V_3O_8/SiO_{2(500\text{-}air)}$ is in accordance with the interaction between $Na_{1+x}V_3O_8$ and the silica surface, likely forming $Na^+\cdots O{=}V(OSi{\equiv})_3$ sites. Consistent with ^{51}V MAS NMR results, no peak of α-$NaVO_3$ is detected in $Na_6V_{10}O_{28}/SiO_{2(500\text{-}air)}$. ^{23}Na MAS NMR of α-$NaVO_3/SiO_{2(500\text{-}air)}$ shows two Na sites, as expected from its crystal structure.[40] However, the two Na peaks broaden and their ratio changes in α-$NaVO_3/SiO_{2(500\text{-}air)}$ compared to that in crystalline α-$NaVO_3$, possibly owing to the interaction of Na^+ with the vanadyl $[VO_4]SiO_2$ sites, as mentioned above.

The Raman spectrum of $Na_6V_{10}O_{28}/SiO_{2(500\text{-}air)}$ shows characteristic bands that are assigned to crystalline β-$NaVO_3$ (945 cm^{-1}, VO_2 symmetric stretching)[38] and sodium trivanadate $Na_{1+x}V_3O_8$ interacting with silica (737 and 804 cm^{-1}). The band at 804 cm^{-1} could be attributed to the V−O−V linkage bridging VO_5 and VO_6 units via a corner-sharing oxygen atom, by analogy to isostructural $Li_{1+x}V_3O_8$ (Figure 1c).[41] However, this band is shifted by 7 cm^{-1} relative to that of the unsupported $Na_{1+x}V_3O_8$ (811 cm^{-1}). In addition, the band at 737 cm^{-1} has a notably higher intensity in $Na_6V_{10}O_{28}/SiO_{2(500\text{-}air)}$ and $Na_{1+x}V_3O_8/SiO_{2(500\text{-}air)}$ than that in crystalline $Na_{1+x}V_3O_8$, which might be due to the interaction of $Na_{1+x}V_3O_8$ with silica. Based on the previous isotope labeling study of $Li_{1+x}V_3O_8$, it is likely that the bands at 737 and 804 cm^{-1} (Figure 1c) originate from vibrational modes involving the sodium ion motion.[42] The characteristic band at 992 cm^{-1} (V=O stretching vibration in VO_5 polyhedra)[41,42] is also observed in $Na_6V_{10}O_{28}/SiO_{2(500\text{-}air)}$, $Na_{1+x}V_3O_8/SiO_{2(500\text{-}air)}$, and unsupported $Na_{1+x}V_3O_8$ (see Figure S3 for the full range spectra).[12] Isolated vanadium oxo (V=O) sites in $[VO_4]/SiO_{2(500\text{-}air)}$ give rise to a sharp peak at 1039 cm^{-1}.[4,15] Such a sharp peak is observed neither in the Raman spectrum of $Na_6V_{10}O_{28}/SiO_{2(500\text{-}air)}$ nor in that of $Na_{1+x}V_3O_8/SiO_{2(500\text{-}air)}$. However, the latter observation does not exclude the presence of $[VO_4]\cdots Na^+$ sites in these two materials.[43]

https://dx.doi.org/10.1021/acscatal.9b04752
ACS Catal. 2020, 10, 2314−2321

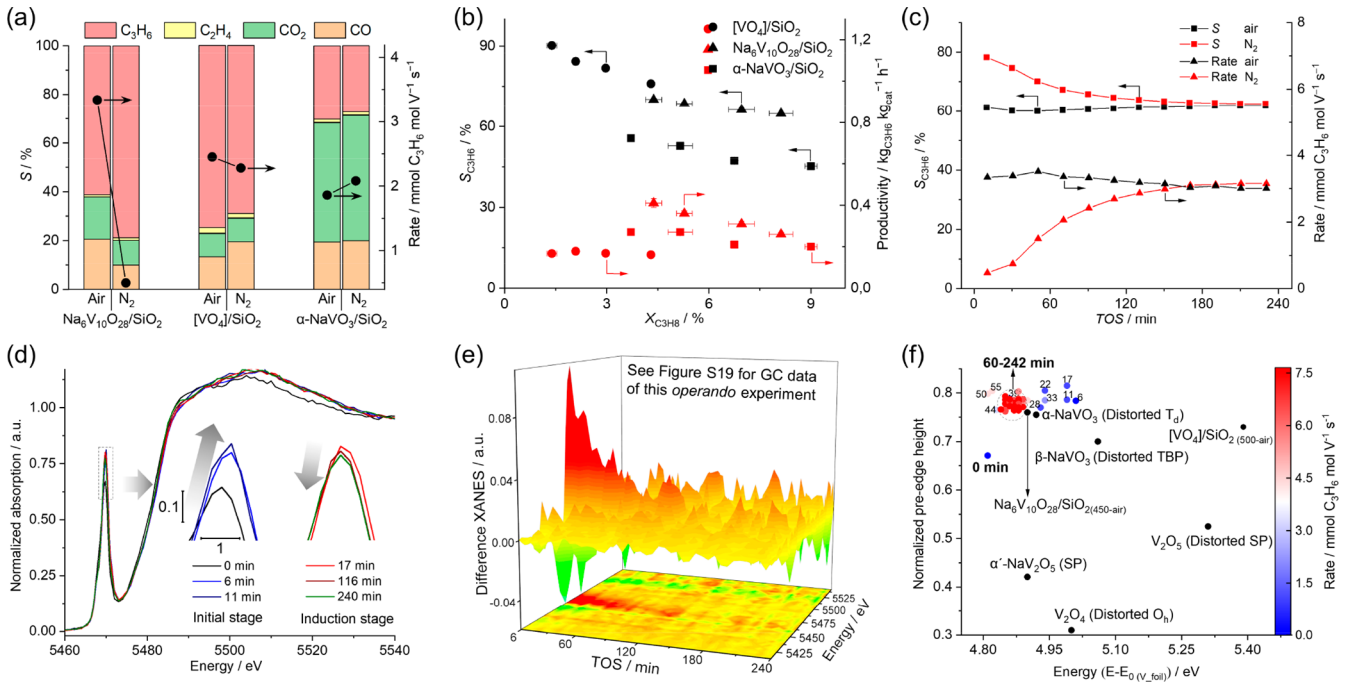

Figure 2. (a) Initial (TOS 10 min) catalytic activity of $Na_6V_{10}O_{28}/SiO_2$, $[VO_4]/SiO_2$, and α-$NaVO_3/SiO_2$ pretreated in air or N_2 in ODP conditions (450 °C, C_3H_8/air = 2:5, WHSV = 6.8 h^{-1}, see Figures S12 and S13 for details); (b) propene selectivity and productivity vs propane conversion for air-treated catalysts (450 °C, 1 h, 21 mL min^{-1} synthetic air) using WHSVs of 5.1, 6.8, 10.2, and 13.6 h^{-1} (450 °C, C_3H_8/air = 2:5); (c) rate and selectivity of propene as a function of TOS for the ODP using $Na_6V_{10}O_{28}/SiO_2$ pretreated in air or N_2; (d) operando XANES spectra under ODP conditions (WHSV = 9.7 h^{-1}) using $Na_6V_{10}O_{28}/SiO_{2(450\text{-}N_2)}$; (e) difference XANES spectra (difference XANES = $spectrum_{TOSmin} - spectrum_{242min}$) in the operando XANES ODP experiment (see Figure S19 for gas chromatography (GC) data) with $Na_6V_{10}O_{28}/SiO_{2(450\text{-}N_2)}$; and (f) relation of the normalized pre-edge height and its absorption energy position to specific activities (colored scale bar) of $Na_6V_{10}O_{28}/SiO_{2(450\text{-}N_2)}$ as a function of TOS and selected references with various V coordination environments and oxidation states.

Transmission electron microscopy (TEM) of $Na_6V_{10}O_{28}/SiO_2$ (exposed to air during the sample transfer) shows that the silica surface contains areas covered with small nanoparticles of ca. 2 nm in diameter, containing V and Na according to line scan analysis and areas without nanoparticles but with homogenously distributed V and Na according to EDX mapping (Figure 1d). We tentatively ascribe the areas of homogeneous distribution of Na and V to $Na_{1+x}V_3O_8$, which is highly dispersed on the surface of silica. Given that the β-$NaVO_3$ phase shows no shifts in ^{51}V MAS NMR and Raman spectroscopy between the unsupported material and $Na_6V_{10}O_{28}/SiO_{2(500\text{-air})}$, and given that β-$NaVO_3$ is detected by these experimental techniques also in $Na_6V_{10}O_{28}/SiO_2$ exposed to air (Figures S3 and S4), the observed nanoparticles are ascribed to β-$NaVO_3$. We note that obtaining high-resolution TEM data from small nanoparticles to confirm their structural assignment was hampered by their sensitivity to high doze rates of the electron beam.

Turning now to X-ray absorption spectroscopy (XAS), the normalized intensity of the pre-edge peak in the V K-edge XANES spectra increases when the symmetry of the ligand sphere around the vanadium atom changes in the following order: octahedral (O_h), distorted octahedral, square pyramidal (SP), distorted tetrahedral, and tetrahedral (T_d, Figure 1e).[12] Therefore, the intensity and the position of the pre-edge peak can be used to probe the (average) coordination environment around the V atom.[12,44] The dependence of the pre-edge peak intensity and its position on the coordination environment of V is shown in Figure S5. The V and Na K-edge XANES spectra of $Na_6V_{10}O_{28}/SiO_2$ are represented well by a linear combination fitting of β-$NaVO_3$ and $Na_{1+x}V_3O_8/SiO_2$ references (Figures S6 and S7), in agreement with the results of NMR and Raman spectroscopy analyses of the dehydrated and hydrated samples. Unsupported β-$NaVO_3$ was chosen as a XANES reference because silica-supported β-$NaVO_3$ transforms to α-$NaVO_3$ after calcination at 600 °C (Figure S8).[38]

To conclude, ssNMR, Raman, TEM, and XANES analyses indicate that $Na_6V_{10}O_{28}/SiO_{2(500\text{-air})}$ and $Na_6V_{10}O_{28}/SiO_2$ materials contain β-$NaVO_3$, likely present in the form of small nanoparticles, as well as sodium trivanadate $Na_{1+x}V_3O_8$ interacting with the silica support in the dehydroxylated material. This interaction likely forms $Na^+\cdots[VO_4]/SiO_2$ species and/or oligomeric vanadia or vanadate structures. While the exact nature of these sites requires a separate study, it should be noted that the calcination of unsupported $Na_6V_{10}O_{28}$ under identical conditions does not lead to β-$NaVO_3$ but instead gives a mixture of $Na_{1+x}V_3O_8$ and α-$NaVO_3$, according to in situ X-ray diffraction (XRD) experiments (Figures S9 and S10), highlighting how the silica support influences the decomposition pathways of $Na_6V_{10}O_{28}$. Figure 1f presents the crystal structures, vanadium coordination environments, and characteristic spectroscopic signatures of the discussed materials and summarizes the analyses above.

Remembering that V sites supposedly undergo a redox cycle during the ODP, we used thermal pretreatment in N_2 at 500 °C as a test to probe the ease of reduction of the prepared V-based materials. We found that the thermal treatment of $Na_6V_{10}O_{28}/SiO_2$ in a N_2 flow (500 °C, 1 h, material denoted $Na_6V_{10}O_{28}/SiO_{2(500\text{-}N_2)}$) induces a redox reaction between β-

https://dx.doi.org/10.1021/acscatal.9b04752
ACS Catal. 2020, 10, 2314−2321

$NaVO_3$ and $Na_{1+x}V_3O_8/SiO_2$ that forms a reduced α'-NaV_2O_5 phase. Raman spectroscopy provides the clearest evidence for the presence of α'-NaV_2O_5 in $Na_6V_{10}O_{28}/SiO_{2(500\text{-}N_2)}$, revealing an intense band at 968 cm^{-1}, characteristic of α'-NaV_2O_5, and no bands owing to $Na_{1+x}V_3O_8$ and β-$NaVO_3$ (Figures 1c and S3).[45−47] However, note that Raman spectroscopy is more sensitive to particles in preference to highly dispersed surface structures due to the lower Raman cross section for the latter species;[39] therefore, some $Na_{1+x}V_3O_8/SiO_2$ may remain in $Na_6V_{10}O_{28}/SiO_{2(500\text{-}N_2)}$. Consistent with these results, ^{51}V MAS NMR shows that $Na_6V_{10}O_{28}/SiO_{2(500\text{-}N_2)}$ contains no peak at −515 ppm, characteristic of β-$NaVO_3$, while a broad peak at ca. −600 ppm shifts to −615 ppm, which is very close to the position of peaks in $Na_{1+x}V_3O_8/SiO_{2(500\text{-air})}$ (Figure 1a). Since we obtained no ^{51}V MAS NMR signal from the unsupported paramagnetic α'-NaV_2O_5,[48] the broad feature at −615 ppm is likely due to remaining $Na_{1+x}V_3O_8/SiO_2$ species that were not paramagnetically bleached by α'-NaV_2O_5. The ^{23}Na MAS NMR spectrum of $Na_6V_{10}O_{28}/SiO_{2(500\text{-}N_2)}$ reveals a new Na environment with a peak position similar to that of α'-NaV_2O_5 (−48 ppm) along with the disappearance of the peak due to β-$NaVO_3$. The intensity of the more deshielded Na environment at −16 ppm in $Na_6V_{10}O_{28}/SiO_{2(500\text{-}N_2)}$ is significantly decreased compared to that in $Na_6V_{10}O_{28}/SiO_{2(500\text{-air})}$ (Figure 1b). According to V K-edge XANES, the in situ-prepared $Na_6V_{10}O_{28}/SiO_{2(450\text{-}N_2)}$ material (here, we used 450 °C, which is the temperature of the catalytic ODP experiment) is more reduced and features a lower normalized height of the pre-edge peak compared to that of $Na_6V_{10}O_{28}/SiO_{2(450\text{-air})}$ (edge energies of 5481.9 and 5482.7 eV and normalized pre-edge peak heights of 0.67−0.76, respectively; Figure 1e). Both changes (intensity and position of the pre-edge feature) are consistent with the formation of reduced α'-NaV_2O_5 with vanadium sites in a square-based pyramid (SP) geometry. In general, α'-NaV_2O_5 features VO_5 units as layers sharing edges and corners in the a−b plane with equivalent V atoms of an average oxidation state of +4.5 (Figure 1f).[48−50] To summarize, our data suggest that β-$NaVO_3$ reacts with dispersed $Na_{1+x}V_3O_8$ in $Na_6V_{10}O_{28}/SiO_2$ when heated up in an inert atmosphere to 450−500 °C, yielding reduced α'-NaV_2O_5 (likely accompanied by the release of oxygen). In contrast to reduction under a N_2 atmosphere that is observed only for $Na_6V_{10}O_{28}/SiO_2$, in the more reducing conditions of H_2 temperature-programmed reduction experiments, all three catalysts are reduced (Figure S11).

The catalytic activity of the prepared materials for the ODP was compared at 450 °C (C_3H_8/air = 2:5, at weight hourly space velocity (WHSV) = 6.8 h^{-1} based on the propane flow rate) using either air or a N_2 pretreatment (Figure 2a). Typical propane conversions at 450 °C were between ca. 1 and 9% for the four WHSVs studied (5.1−13.6 h^{-1}). At the same conversion (4.3%), $Na_6V_{10}O_{28}/SiO_{2(500\text{-air})}$ showed a higher productivity (0.41 $kg_{C_3H_6}$ kg_{cat}^{-1} h^{-1}) compared to that of $[VO_4]/SiO_2$ (0.16 $kg_{C_3H_6}$ kg_{cat}^{-1} h^{-1}) at a slightly lower selectivity (70 vs 76%, Figure 2b). It is worth mentioning that our selectivity and productivity data for the benchmark catalyst $[VO_4]/SiO_2$, presented in Figure 2b, match well the literature data for this catalyst.[2] Interestingly, we observe that $Na_6V_{10}O_{28}/SiO_{2(450\text{-}N_2)}$ has a significantly lower initial specific activity compared to that of $Na_6V_{10}O_{28}/SiO_{2(450\text{-air})}$ (ca. 0.5 vs 3.3 mmol C_3H_6 mol V^{-1} s^{-1} with respective selectivities to propene at 79 and 62%, Figure 2a). We tentatively ascribe the high selectivity to propene (at a low conversion of ca. 1.5%) to remaining small amounts of highly dispersed $Na_{1+x}V_3O_8$ sites on silica. However, the activity of $Na_6V_{10}O_{28}/SiO_{2(450\text{-}N_2)}$ increases with time on stream, while the selectivity to propene drops, reaching the performance of $Na_6V_{10}O_{28}/SiO_{2(450\text{-air})}$ after ca. 3 h, both in terms of propane conversion and propene selectivity (Figure 2c). This catalytic data suggests the evolution of α'-NaV_2O_5 in $Na_6V_{10}O_{28}/SiO_{2(450\text{-}N_2)}$ to the same active species as those in $Na_6V_{10}O_{28}/SiO_{2(450\text{-air})}$. Comparison of the ^{51}V and ^{23}Na MAS NMR spectra of $Na_6V_{10}O_{28}/SiO_{2(450\text{-air})}$ and $Na_6V_{10}O_{28}/SiO_{2(450\text{-}N_2)}$ after 4 h TOS reveals features of β-$NaVO_3$ and $Na_{1+x}V_3O_8/SiO_2$ (Figures S12 and S13). As the reaction mixture contains both a reductant (hydrocarbons, CO) and an oxidant (O_2), an additional catalytic test was performed using only air treatment after the N_2 pretreatment to verify whether the catalytic activity of the calcined sample would be recovered faster after air treatment. Indeed, the exposure of $Na_6V_{10}O_{28}/SiO_{2(450\text{-}N_2)}$ to air for 1 h at 450 °C completely recovers the catalytic activity, reforming β-$NaVO_3$ and $Na_{1+x}V_3O_8/SiO_2$ (see Figures S14 and S15 for catalytic and Raman spectra, respectively).

In a sharp contrast, α-$NaVO_3/SiO_2$ and the reference catalyst $[VO_4]/SiO_2$ show little change in activity or selectivity in ODP, displaying stable performances independent of the pretreatment conditions (at an identical nominal V coverage of ca. 1 V nm^{-2}; see Figure 2a for the initial activity and Figures S16 and S17 for changes of activity and selectivity with TOS). Furthermore, according to Raman spectroscopy, neither α-$NaVO_3/SiO_2$ nor $[VO_4]/SiO_2$ undergoes structural changes upon N_2 treatment at 450 °C (Figure S18). Among the air-pretreated catalysts, $[VO_4]/SiO_2$ has the highest selectivity toward propene (74% at 2.5 mmol C_3H_6 mol V^{-1} s^{-1}), while α-$NaVO_3/SiO_2$ shows the lowest initial activity and propene selectivity (1.8 mmol C_3H_6 mol V^{-1} s^{-1} and 30%, respectively, Figure 2a).

To obtain insight into the evolution of the oxidation state and coordination environment of vanadium during the activation period of $Na_6V_{10}O_{28}/SiO_{2(450\text{-}N_2)}$ under ODP conditions, an operando V K-edge XANES experiment was conducted using a capillary flow reactor while monitoring the composition of the effluent gas with a compact GC and a time resolution of 3 min per chromatogram (WHSV ca. 9.7 h^{-1}, Figure 2d−f). Exposure of $Na_6V_{10}O_{28}/SiO_{2(450\text{-}N_2)}$ to the feed gas at 450 °C rapidly shifts the edge position to higher energies (from 5481.9 to 5482.6 eV) and increases the normalized pre-edge peak height (from 0.67 to 0.81) within the first 12 min of TOS (initial stage, Figure 2d). This is explained by the fast reoxidation of α'-NaV_2O_5 to $Na_{1+x}V_3O_8/SiO_2$ and β-$NaVO_3$. After this rapid reoxidation, the catalytic activity continues to rise with TOS, approximately for the next 3 h. Overall, the operando XAS results are very similar to the experiment in a laboratory packed-bed reactor that used a lower WHSV of 6.8 h^{-1} (Figure 2c and Figure S19). The changes in the XANES spectra with TOS after 12 min are very subtle and, yet, can be visualized by the difference XANES spectra obtained by subtracting the current XANES spectrum from the last spectrum in the operando experiment, i.e., after TOS = 242 min at the point of maximum activity (Figure 2e). The

https://dx.doi.org/10.1021/acscatal.9b04752
ACS Catal. 2020, 10, 2314−2321

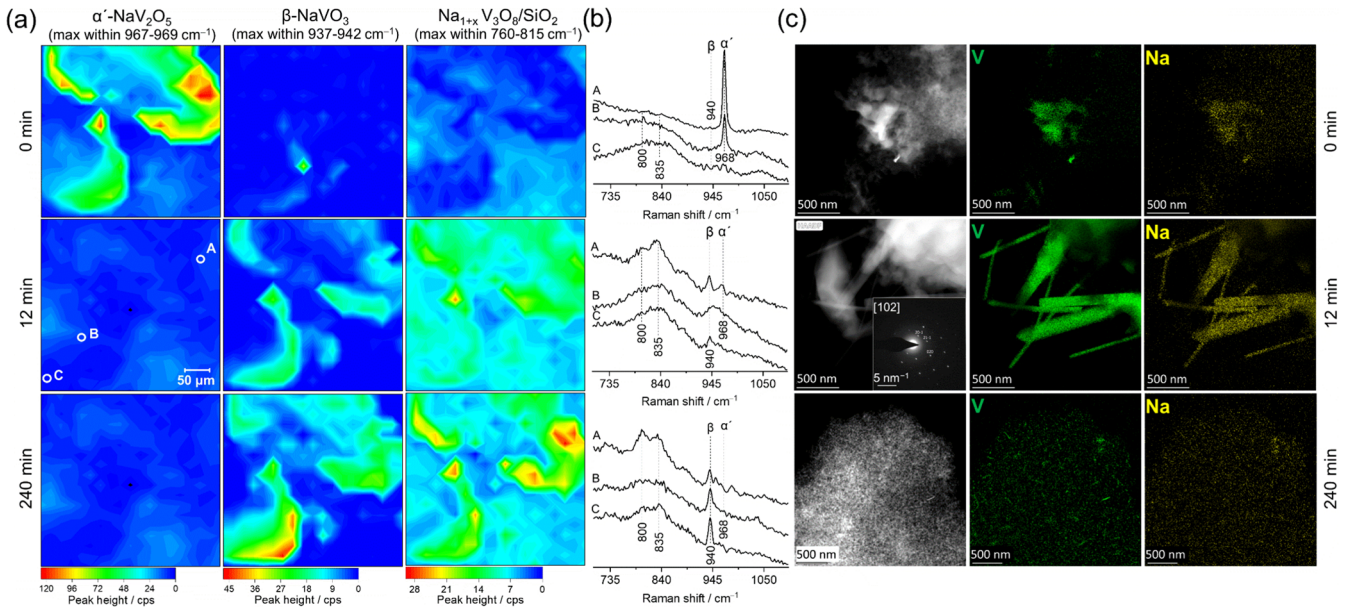

Figure 3. (a) In situ Raman mapping (after cooling down to room temperature) of $Na_6V_{10}O_{28}/SiO_{2(450\text{-}N_2)}$ with TOS of the ODP of propane; (b) Raman spectra at selected points (A, B, and C; for locations, see the middle left panel in (a)); and (c) TEM-EDX of $Na_6V_{10}O_{28}/SiO_{2(450\text{-}N_2)}$ at 0, 12, and 240 min TOS at 450 °C, propane/air = 2:5, and total flow rates of 2.1 and 21 mL min^{-1} for the in situ Raman and catalytic experiments, respectively. For each measurement, a fresh $Na_6V_{10}O_{28}/SiO_{2(450\text{-}N_2)}$ catalyst was used and the reacted catalysts were cooled down to room temperature under a reactive gas atmosphere.

coordination environment of the V atom and its correlation to the pre-edge peak height and absorption energy position indicate that $Na_6V_{10}O_{28}/SiO_{2(450\text{-}N_2)}$ evolves in the ODP experiment, reaching ultimately values that are typical for vanadate ions in a distorted T_d environment (Figure 2f). Overall, the operando XANES experiment suggests that the local structure of the V atoms in $Na_6V_{10}O_{28}/SiO_{2(450\text{-}N_2)}$ changes rapidly with TOS, consistent with the fast reformation of oxidized $Na_{1+x}V_3O_8$ and β-$NaVO_3$ species. As a consequence, it is conceivable that the significantly slower process that is responsible for the restoration of the catalytic activity of $Na_6V_{10}O_{28}/SiO_{2(450\text{-}N_2)}$ proceeds at a different length scale (nano/micrometer rather than atomic scale) and possibly involves changes in the dispersion of vanadium species on the silica support.

To probe the validity of this hypothesis, we followed the structural evolution of $Na_6V_{10}O_{28}/SiO_{2(450\text{-}N_2)}$ during the ODP using in situ Raman mapping (Linkam CCR1000 cell maintained at 450 °C for 12 and 240 min under a reactive gas flow, Figure 3a). In total, 342 points (380 × 360 μm^2) separated by 20 μm were used, and Raman maps were prepared based on the intensity of the characteristic peaks of α'-NaV_2O_5, β-$NaVO_3$, and $Na_{1+x}V_3O_8/SiO_2$ phases (Figure 3b). The intensity of the Raman band in the range of 967−969 cm^{-1} was used for the mapping of the α'-NaV_2O_5 phase. The maximal intensities of Raman bands in the ranges of 937−942 and 760−815 cm^{-1} were used for the β-$NaVO_3$ and $Na_{1+x}V_3O_8/SiO_2$ species, respectively. For higher signal-to-noise ratios, all spectra were acquired at room temperature (RT) after cooling down the catalyst under ODP conditions and switching to a N_2 atmosphere at room temperature (RT) for data acquisition. Due to the adsorption of water produced during ODP on the catalyst surface upon cooling to RT, there is a 3−5 cm^{-1} red shift in the bands of β-$NaVO_3$ phase and a 20−65 cm^{-1} blue shift for the bands of $Na_{1+x}V_3O_8$ species (Figure 3b). The intense Raman signal due to α'-NaV_2O_5 in $Na_6V_{10}O_{28}/SiO_{2(450\text{-}N_2)}$ disappears completely after 12 min TOS, in agreement with the fast oxidation of $Na_6V_{10}O_{28}/SiO_{2(450\text{-}N_2)}$ observed by operando XANES. The disappearance of α'-NaV_2O_5 after 12 min TOS coincides with the formation of β-$NaVO_3$ as well as $Na_{1+x}V_3O_8/SiO_2$. After 240 min TOS, the signal intensities due to β-$NaVO_3$ and $Na_{1+x}V_3O_8/SiO_2$ had increased, suggesting a higher dispersion at this point.

Following the morphological evolution of $Na_6V_{10}O_{28}/SiO_{2(450\text{-}N_2)}$ with TOS by ex situ TEM-EDX mapping with selected-area electron diffraction (SAED) reveals that $Na_6V_{10}O_{28}/SiO_{2(450\text{-}N_2)}$ (0 min TOS, i.e., directly after the N_2 pretreatment) contains an agglomerated phase containing Na and V, which is assigned to α'-NaV_2O_5 based on the spectroscopic characterization discussed above (Figure 3c, top panel). After 12 min TOS, associated with a partial recovery of the catalytic activity, nano- and even microsized rods appear on the silica support (Figure 3c, middle panel). SAED analysis of such a crystal reveals that its diffraction pattern can be indexed to that of $Na_{1.164}V_3O_8$ oriented along the [102] zone axis (Figure 3c, middle panel and inset, and Figure S20). While the formation of microsized rods clearly indicates a poor dispersion of the trivanadate phase after 12 min TOS, we note that both Raman spectroscopy and EDX mapping were performed at room temperature, which might have exacerbated the poor dispersion due to crystal growth while cooling down the specimen to room temperature. However, after 240 min TOS, the rods had nearly disappeared (only scarce nanorods of ca. 100 nm were detected during the survey of various specimen areas), confirming that the redispersion of Na and V took place on the silica support during the 3 h activation stage. These results of Raman spectroscopy and TEM-EDX mapping are also consistent with

https://dx.doi.org/10.1021/acscatal.9b04752
ACS Catal. 2020, 10, 2314−2321

similar ^{21}Na and ^{51}V ssNMR spectra of $Na_6V_{10}O_{28}/SiO_{2(450\text{-}N_2)}$ and $Na_6V_{10}O_{28}/SiO_{2(450\text{-air})}$ after 240 min TOS.

CONCLUSIONS

In summary, the calcination in air of the sodium decavanadate precursor $Na_6V_{10}O_{28}$ on SiO_2 yielded the metastable β-$NaVO_3$ phase and $Na_{1+x}V_3O_8$ interacting with the silica support. This catalyst exceeds the activity of the reference catalysts $[VO_4]/SiO_2$ and α-$NaVO_3/SiO_2$ by 24 and 45%, respectively. In contrast to α-$NaVO_3/SiO_2$ and $[VO_4]/SiO_2$ that are structurally stable under inert gas conditions, β-$NaVO_3$ and $Na_{1+x}V_3O_8/SiO_2$ in $Na_6V_{10}O_{28}/SiO_2$ react when heated to 450−500 °C under N_2, yielding a reduced phase, α'-NaV_2O_5. This process is reversible, and under the conditions of oxidative dehydrogenation of propane or in air, α'-NaV_2O_5 transforms back to β-$NaVO_3$ and $Na_{1+x}V_3O_8/SiO_2$. However, the oxidation under ODP conditions occurs rapidly, within 12 min, and gives large crystallites of $Na_{1+x}V_3O_8$ that slowly redisperse on the support with TOS (ca. 3 h), increasing the number of the exposed active sites and thereby enhancing catalytic activity. Our results confirm the key roles of dispersion and reducibility; the latter is relevant, given the redox mechanism of the ODP reaction on vanadium-based ODP catalysts. The work to delineate the contributions from $Na_{1+x}V_3O_8/SiO_2$ and β-$NaVO_3$ to the enhanced activity of $Na_6V_{10}O_{28}/SiO_2$ is currently underway in our laboratory.

ASSOCIATED CONTENT

Supporting Information

The Supporting Information is available free of charge at https://pubs.acs.org/doi/10.1021/acscatal.9b04752.

Experimental details; diffractograms of reference materials and $Na_6V_{10}O_{28}\cdot 18H_2O$; H_2 temperature programmed reduction of studied catalysts; composition of the effluent; SAED of a nanorod; propene selectivity and productivity; oxygen conversions and CO/CO_2 molar ratios; and V and Na K-edge XANES, XRD, NMR, Raman, XAS, DSC, TGA, DRIFT, and TEM data (PDF)

AUTHOR INFORMATION

Corresponding Authors

Alexey Fedorov − *Laboratory of Energy Science and Engineering, Department of Mechanical and Process Engineering, ETH Zürich, CH-8092 Zürich, Switzerland;* orcid.org/0000-0001-9814-6726; Email: fedoroal@ethz.ch

Christoph R. Müller − *Laboratory of Energy Science and Engineering, Department of Mechanical and Process Engineering, ETH Zürich, CH-8092 Zürich, Switzerland;* orcid.org/0000-0003-2234-6902; Email: muelchri@ethz.ch

Authors

Manouchehr Nadjafi − *Laboratory of Energy Science and Engineering, Department of Mechanical and Process Engineering, ETH Zürich, CH-8092 Zürich, Switzerland*

Paula M. Abdala − *Laboratory of Energy Science and Engineering, Department of Mechanical and Process Engineering, ETH Zürich, CH-8092 Zürich, Switzerland;* orcid.org/0000-0002-2011-1707

Rene Verel − *Laboratory of Inorganic Chemistry, Department of Chemistry and Applied Biosciences, ETH Zürich, CH-8093 Zürich, Switzerland;* orcid.org/0000-0003-1575-2232

Davood Hosseini − *Laboratory of Energy Science and Engineering, Department of Mechanical and Process Engineering, ETH Zürich, CH-8092 Zürich, Switzerland;* orcid.org/0000-0001-5261-3149

Olga V. Safonova − *Division of Energy and Environment, Paul Scherrer Institute, CH-5232 Villigen, Switzerland;* orcid.org/0000-0002-6772-1414

Complete contact information is available at: https://pubs.acs.org/10.1021/acscatal.9b04752

Notes

The authors declare no competing financial interest.

ACKNOWLEDGMENTS

Dr. Agnieszka Kierzkowska (ETH Zürich) is gratefully acknowledged for the electron microscopy and the ICP work. We thank the Scientific Centre for Optical and Electron Microscopy (ScopeM) for providing access to electron microscopes. The Paul Scherer Institute (PSI), SuperXAS, and Phoenix beamlines are acknowledged for providing access to synchrotron facilities.

REFERENCES

(1) Sattler, J. J. H. B.; Ruiz-Martinez, J.; Santillan-Jimenez, E.; Weckhuysen, B. M. Catalytic Dehydrogenation of Light Alkanes on Metals and Metal Oxides. *Chem. Rev.* **2014**, *114*, 10613−10653.

(2) Grant, J. T.; Carrero, C. A.; Goeltl, F.; Venegas, J.; Mueller, P.; Burt, S. P.; Specht, S. E.; McDermott, W. P.; Chieregato, A.; Hermans, I. Selective oxidative dehydrogenation of propane to propene using boron nitride catalysts. *Science* **2016**, *354*, 1570−1573.

(3) Carrero, C. A.; Schloegl, R.; Wachs, I. E.; Schomaecker, R. Critical Literature Review of the Kinetics for the Oxidative Dehydrogenation of Propane over Well-Defined Supported Vanadium Oxide Catalysts. *ACS Catal.* **2014**, *4*, 3357−3380.

(4) Coperet, C. C−H Bond Activation and Organometallic Intermediates on Isolated Metal Centers on Oxide Surfaces. *Chem. Rev.* **2010**, *110*, 656−680.

(5) Langeslay, R. R.; Kaphan, D. M.; Marshall, C. L.; Stair, P. C.; Sattelberger, A. P.; Delferro, M. Catalytic Applications of Vanadium: A Mechanistic Perspective. *Chem. Rev.* **2019**, *119*, 2128−2191.

(6) Eckert, H.; Deo, G.; Wachs, I. E.; Hirt, A. M. Solid state ^{51}V NMR structural studies of vanadium(V) oxide catalysts supported on TiO_2(anatase) and TiO_2(rutile). The influence of surface impurities on the vanadium(V) coordination. *Colloids Surf.* **1990**, *45*, 347−359.

(7) Lapina, O. B.; Mastikhin, V. M.; Simonova, L. G.; Bulgakova, Y. O. Characterization of surface species of supported V_2O_5/Al_2O_3 catalysts by ^{51}V NMR. *J. Mol. Catal.* **1991**, *69*, 61−73.

(8) Das, N.; Eckert, H.; Hu, H.; Wachs, I. E.; Walzer, J. F.; Feher, F. J. Bonding states of surface vanadium(V) oxide phases on silica: structural characterization by vanadium-51 NMR and Raman spectroscopy. *J. Phys. Chem. A.* **1993**, *97*, 8240−8243.

(9) Jaegers, N. R.; Lai, J.-K.; He, Y.; Walter, E.; Dixon, D. A.; Vasiliu, M.; Chen, Y.; Wang, C.; Hu, M. Y.; Mueller, K. T.; Wachs, I. E.; Wang, Y.; Hu, J. Z. Mechanism by which Tungsten Oxide Promotes the Activity of Supported V_2O_5/TiO_2 Catalysts for NO_X Abatement: Structural Effects Revealed by ^{51}V MAS NMR Spectroscopy. *Angew. Chem.* **2019**, *131*, 12739−12746.

(10) Jaegers, N. R.; Wan, C.; Hu, M. Y.; Vasiliu, M.; Dixon, D. A.; Walter, E.; Wachs, I. E.; Wang, Y.; Hu, J. Z. Investigation of Silica-Supported Vanadium Oxide Catalysts by High-Field ^{51}V Magic-Angle Spinning NMR. *J. Phys. Chem. C* **2017**, *121*, 6246−6254.

(11) Tanaka, T.; Yamashita, H.; Tsuchitani, R.; Funabiki, T.; Yoshida, S. X-ray absorption (EXAFS/XANES) study of supported

vanadium oxide catalysts. Structure of surface vanadium oxide species on silica and γ-alumina at a low level of vanadium loading. *J. Chem. Soc., Faraday Trans. 1* **1988**, *84*, 2987−2999.
(12) Gao, X.; Bare, S. R.; Weckhuysen, B. M.; Wachs, I. E. In Situ Spectroscopic Investigation of Molecular Structures of Highly Dispersed Vanadium Oxide on Silica under Various Conditions. *J. Phys. Chem. B* **1998**, *102*, 10842−10852.
(13) Gao, X.; Bañares, M. A.; Wachs, I. E. Ethane and n-Butane Oxidation over Supported Vanadium Oxide Catalysts: An in Situ UV−Visible Diffuse Reflectance Spectroscopic Investigation. *J. Catal.* **1999**, *188*, 325−331.
(14) Gao, X.; Wachs, I. E. Investigation of Surface Structures of Supported Vanadium Oxide Catalysts by UV−vis−NIR Diffuse Reflectance Spectroscopy. *J. Phys. Chem. B* **2000**, *104*, 1261−1268.
(15) Lee, E. L.; Wachs, I. E. In Situ Raman Spectroscopy of SiO_2-Supported Transition Metal Oxide Catalysts: An Isotopic $^{18}O-^{16}O$ Exchange Study. *J. Phys. Chem. C* **2008**, *112*, 6487−6498.
(16) Oyama, S. T.; Went, G. T.; Lewis, K. B.; Bell, A. T.; Somorjai, G. A. Oxygen chemisorption and laser Raman spectroscopy of unsupported and silica-supported vanadium oxide catalysts. *J. Phys. Chem. A.* **1989**, *93*, 6786−6790.
(17) Love, A. M.; Carrero, C. A.; Chieregato, A.; Grant, J. T.; Conrad, S.; Verel, R.; Hermans, I. Elucidation of Anchoring and Restructuring Steps during Synthesis of Silica-Supported Vanadium Oxide Catalysts. *Chem. Mater.* **2016**, *28*, 5495−5504.
(18) Wachs, I. E. Catalysis science of supported vanadium oxide catalysts. *Dalton Trans.* **2013**, *42*, 11762−11769.
(19) Grant, J. T.; Carrero, C. A.; Love, A. M.; Verel, R.; Hermans, I. Enhanced Two-Dimensional Dispersion of Group V Metal Oxides on Silica. *ACS Catal.* **2015**, *5*, 5787−5793.
(20) Carrero, C. A.; Keturakis, C. J.; Orrego, A.; Schomacker, R.; Wachs, I. E. Anomalous reactivity of supported V_2O_5 nanoparticles for propane oxidative dehydrogenation: influence of the vanadium oxide precursor. *Dalton Trans.* **2013**, *42*, 12644−12653.
(21) Deo, G.; Wachs, I. E. Reactivity of Supported Vanadium Oxide Catalysts: The Partial Oxidation of Methanol. *J. Catal.* **1994**, *146*, 323−334.
(22) Tian, H.; Ross, E. I.; Wachs, I. E. Quantitative Determination of the Speciation of Surface Vanadium Oxides and Their Catalytic Activity. *J. Phys. Chem. B* **2006**, *110*, 9593−9600.
(23) Vuurman, M. A.; Wachs, I. E. In situ Raman spectroscopy of alumina-supported metal oxide catalysts. *J. Phys. Chem. A.* **1992**, *96*, 5008−5016.
(24) Khodakov, A.; Olthof, B.; Bell, A. T.; Iglesia, E. Structure and Catalytic Properties of Supported Vanadium Oxides: Support Effects on Oxidative Dehydrogenation Reactions. *J. Catal.* **1999**, *181*, 205−216.
(25) Schimmoeller, B.; Jiang, Y.; Pratsinis, S. E.; Baiker, A. Structure of flame-made vanadia/silica and catalytic behavior in the oxidative dehydrogenation of propane. *J. Catal.* **2010**, *274*, 64−75.
(26) Grant, J. T.; Love, A. M.; Carrero, C. A.; Huang, F.; Panger, J.; Verel, R.; Hermans, I. Improved supported metal oxides for the oxidative dehydrogenation of propane. *Top. Catal.* **2016**, *59*, 1545−1553.
(27) Lemonidou, A. A.; Nalbandian, L.; Vasalos, I. A. Oxidative dehydrogenation of propane over vanadium oxide based catalysts: Effect of support and alkali promoter. *Catal. Today* **2000**, *61*, 333−341.
(28) Mars, P.; van Krevelen, D. W. Oxidations carried out by means of vanadium oxide catalysts. *Chem. Eng. Sci.* **1954**, *3*, 41−59.
(29) Cheng, M. J.; Chenoweth, K.; Oxgaard, J.; van Duin, A.; Goddard, W. A. Single-Site Vanadyl Activation, Functionalization, and Reoxidation Reaction Mechanism for Propane Oxidative Dehydrogenation on the Cubic V_4O_{10} Cluster. *J. Phys. Chem. C* **2007**, *111*, 5115−5127.
(30) Rozanska, X.; Fortrie, R.; Sauer, J. Size-Dependent Catalytic Activity of Supported Vanadium Oxide Species: Oxidative Dehydrogenation of Propane. *J. Am. Chem. Soc.* **2014**, *136*, 7751−7761.
(31) Rozanska, X.; Fortrie, R.; Sauer, J. Oxidative Dehydrogenation of Propane by Monomeric Vanadium Oxide Sites on Silica Support. *J. Phys. Chem. C* **2007**, *111*, 6041−6050.
(32) Beck, B.; Harth, M.; Hamilton, N. G.; Carrero, C.; Uhlrich, J. J.; Trunschke, A.; Shaikhutdinov, S.; Schubert, H.; Freund, H.-J.; Schlögl, R.; Sauer, J.; Schomäcker, R. Partial oxidation of ethanol on vanadia catalysts on supporting oxides with different redox properties compared to propane. *J. Catal.* **2012**, *296*, 120−131.
(33) Alexopoulos, K.; Reyniers, M.-F.; Marin, G. B. Reaction path analysis of propane selective oxidation over V_2O_5 and V_2O_5/TiO_2. *J. Catal.* **2012**, *289*, 127−139.
(34) Zhao, Z. J.; Tengfang, W.; Chuanye, X.; Guodong, S.; Rentao, M.; Liang, Z.; Jinlong, G. Hydroxyl-Mediated Non-oxidative Propane Dehydrogenation over VO_x/γ-Al_2O_3 Catalysts with Improved Stability. *Angew. Chem., Int. Ed.* **2018**, *57*, 6791−6795.
(35) Liu, G.; Zhao, Z.-J.; Wu, T.; Zeng, L.; Gong, J. Nature of the Active Sites of VO_x/Al_2O_3 Catalysts for Propane Dehydrogenation. *ACS Catal.* **2016**, *6*, 5207−5214.
(36) Chen, K.; Khodakov, A.; Yang, J.; Bell, A. T.; Iglesia, E. Isotopic Tracer and Kinetic Studies of Oxidative Dehydrogenation Pathways on Vanadium Oxide Catalysts. *J. Catal.* **1999**, *186*, 325−333.
(37) Li, Y.; Wei, Z.; Sun, J.; Gao, F.; Peden, C. H. F.; Wang, Y. Effect of Sodium on the Catalytic Properties of VO_x/CeO_2 Catalysts for Oxidative Dehydrogenation of Methanol. *J Phys. Chem. C* **2013**, *117*, 5722−5729.
(38) Seetharaman, S.; Bhat, H. L.; Narayanan, P. S. Raman spectroscopic studies on sodium metavanadate. *J. Raman Spectrosc.* **1983**, *14*, 401−405.
(39) Xie, S.; Iglesia, E.; Bell, A. T. Effects of Hydration and Dehydration on the Structure of Silica-Supported Vanadia Species. *Langmuir* **2000**, *16*, 7162−7167.
(40) Skibsted, J.; Nielsen, N. C.; Bildsoe, H.; Jakobsen, H. J. Magnitudes and relative orientation of ^{51}V quadrupole coupling and anisotropic shielding tensors in metavanadates and potassium vanadium oxide (KV_3O_8) from ^{51}V MAS NMR spectra. ^{23}Na quadrupole coupling parameters for α- and β-$NaVO_3$. *J. Am. Chem. Soc.* **1993**, *115*, 7351−7362.
(41) Yang, G.; Wang, G.; Hou, W. Microwave Solid-State Synthesis of LiV_3O_8 as Cathode Material for Lithium Batteries. *J. Phys. Chem. B* **2005**, *109*, 11186−11196.
(42) Zhang, X.; Frech, R. Spectroscopic investigation of $Li_{1+x}V_3O_8$. *Electrochim. Acta* **1998**, *43*, 861−868.
(43) Takenaka, S.; Tanaka, T.; Yamazaki, T.; Funabiki, T.; Yoshida, S. Structure of Active Species in Alkali-Ion-Modified Silica-Supported Vanadium Oxide. *J. Phys. Chem. B* **1997**, *101*, 9035−9040.
(44) Wong, J.; Lytle, F. W.; Messmer, R. P.; Maylotte, D. H. K-edge absorption spectra of selected vanadium compounds. *Phys. Rev. B* **1984**, *30*, 5596−5610.
(45) Li, W.; Huang, J.; Cao, L.; Liu, Y.; Pan, L.; Feng, L. In Situ Topology Synthesis of Orthorhombic NaV_2O_5 with High Pseudocapacitive Contribution for Lithium-Ion Battery Anode. *ACS Sustainable Chem. Eng.* **2019**, *7*, 94−99.
(46) Liu, P.; Zhu, K.; Bian, K.; Xu, Y.; Zhang, F.; Zhang, W.; Huang, W.; Zhang, J. One-step and short-time synthesis of 3D NaV_2O_5 mesocrystal as anode materials of Na-Ion batteries. *J. Power Sources* **2018**, *395*, 158−162.
(47) Liu, P.; Zhou, D.; Zhu, K.; Wu, Q.; Wang, Y.; Tai, G.; Zhang, W.; Gu, Q. Bundle-like α′-NaV_2O_5 mesocrystals: from synthesis, growth mechanism to analysis of Na-ion intercalation/deintercalation abilities. *Nanoscale* **2016**, *8*, 1975−1985.
(48) Zvyagin, A. A. Temperature dependence of the electron paramagnetic resonance linewidth in NaV_2O_5. *Phys. Rev. B* **2001**, *63*, No. 172409.
(49) Gaulin, B. D.; Lumsden, M. D.; Kremer, R. K.; Lumsden, M. A.; Dabkowska, H. Two Dimensional Ordering and Fluctuations in α′-NaV_2O_5. *Phys. Rev. Lett.* **2000**, *84*, 3446−3449.
(50) Smolinski, H.; Gros, C.; Weber, W.; Peuchert, U.; Roth, G.; Weiden, M.; Geibel, C. NaV_2O_5 as a Quarter-Filled Ladder Compound. *Phys. Rev. Lett.* **1998**, *80*, 5164−5167.

https://dx.doi.org/10.1021/acscatal.9b04752
ACS Catal. 2020, 10, 2314−2321